CHALMERS

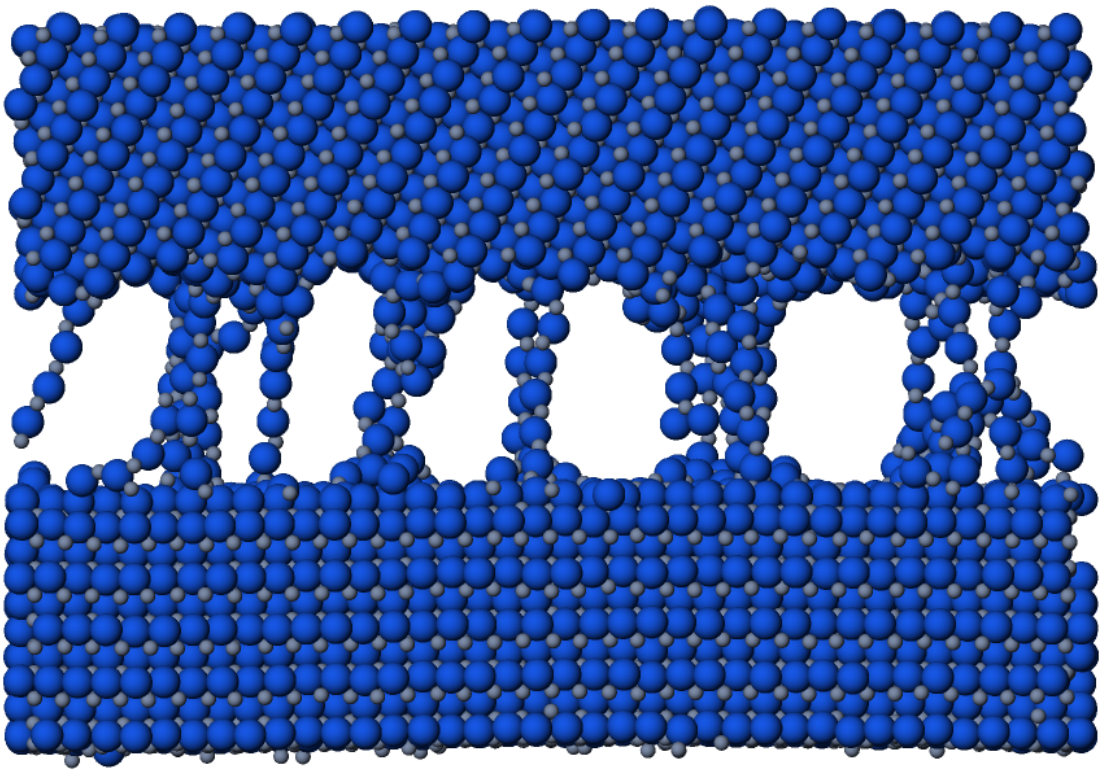

Molecular Dynamics Simulations of Grain Boundaries in Cemented Carbides

MARTIN GREN

Department of Applied Physics
CHALMERS UNIVERSITY OF TECHNOLOGY
Gothenburg, Sweden 2013

THESIS FOR THE DEGREE OF MASTER OF SCIENCE

Molecular Dynamics Simulations of Grain Boundaries in Cemented Carbides

Martin Gren

CHALMERS

Department of Applied Physics
Chalmers University of Technology
Gothenburg, Sweden 2013

Molecular Dynamics Simulations of Grain Boundaries in Cemented Carbides

Martin Gren

Department of Applied Physics
Chalmers University of Technology
SE-41296 Göteborg
Sweden
Telephone + 46 (0)31-772 1000

Printed at Chalmers Reproservice
Göteborg, Sweden 2013

Abstract

Cemented carbide is a tool material used in metal machining in industry. It is a composite material based on a mixture of a hard carbide phase and a more though metal binder phase. When used in cutting applications, the productivity is often limited by high temperature plastic deformation. A suggested mechanism for this deformation is grain boundary sliding and separation. In the present thesis grain boundary sliding and separation are studied for the tungsten carbide (WC) – cobalt (Co) system. Clean WC/WC grain boundaries and WC/WC grain boundaries with half a monolayer of segregated Co is investigated. The simulation method used in the thesis is molecular dynamics using a three body analytical bond order potential. The grain boundary sliding and separation was performed using a constant strain rate. The stresses under sliding and separation were found to be on the order of 1–10 GPa. Furthermore, other studies have shown that the stresses are substantially reduced for grain boundaries with several layers of Co, i.e. thin films of Co. The occurrence of grain boundaries with thin films of Co is therefore likely to be crucial for the plastic deformation in WC–Co.

Acknowledgements

I would first like to express my gratitude to my supervisor Göran Wahnström for the opportunity to do my thesis in the Materials and Surface Theory group and for being a supportive and helpful supervisor. Many thanks to my co-workers Martin Petisme and Sven Johansson for always being helpful and cooperative. I would also like to thank my friend Kristoffer Carlsson whose thesis work on mesoscopic simulations including grain boundary mechanisms has given more value to my own thesis by putting it into to a larger context.

Contents

1. Introduction

Cemented carbides, or hardmetals, are with their hardness and toughness very important in tools used in metal machining such as cutting, milling, drilling, and turning [1, 2]. These materials are composites which consist of a heterogeneous mixture of a transition metal carbide and a metal binder. The carbide makes up a hard phase skeleton that lies in a metal binder matrix. In figure 1.1 the structure of the cemented carbide WC–Co can be seen. The positive properties of the different components are superimposed to give a unique combination of toughness and high hardness. Cemented carbides are powder metallurgical products produced by liquid phase sintering.

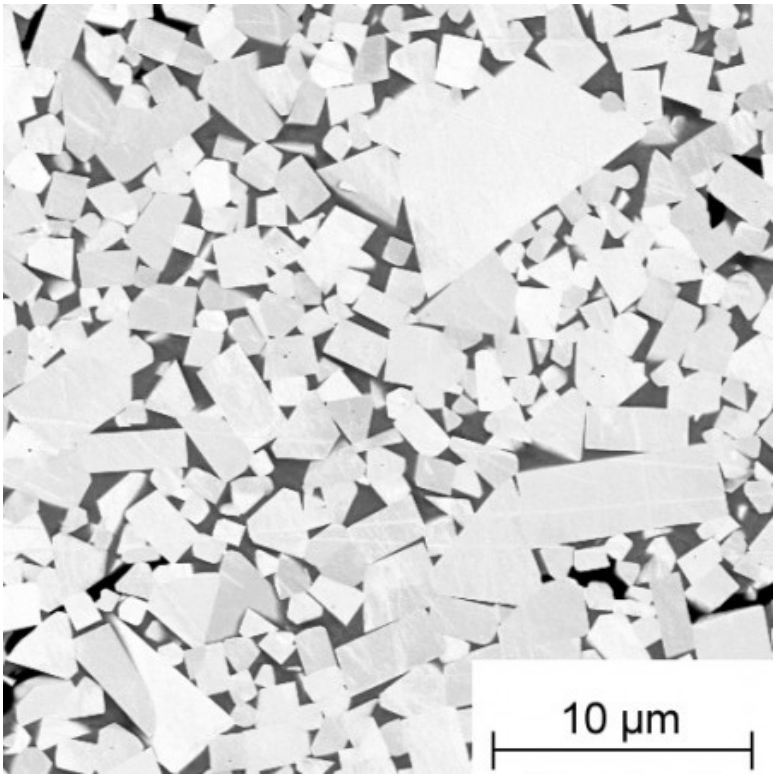

Figure 1.1: Scanning electron microscope image of the grain structure of WC–Co [3].

This thesis will consider the cemented carbide WC–Co without any additions, i.e. tungsten carbide with cobalt as metal binder. A problem with WC–Co is that it deforms plastically under high stresses and temperatures that arise during for example turning [4]. A plastically deformed tool made of WC–Co needs to be replaced and this limits the productivity. A

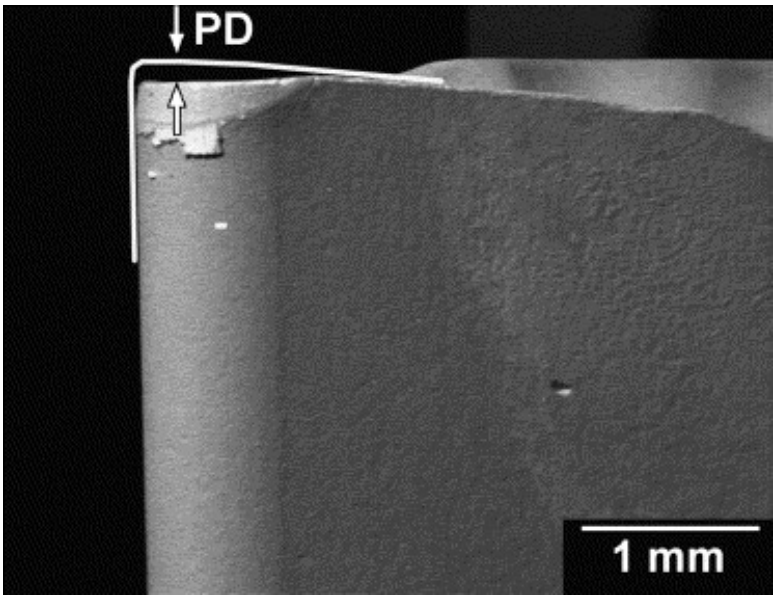

Figure 1.2: A plastically deformed cutting edge of a turning tool based on WC–Co [4].

plastically deformed tool can be seen in figure 1.2. The plastic deformation can involve both deformation in the hard phase skeleton and the binder phase. Experiments have shown that the hard phase WC skeleton is partly broken up when WC–Co is plastically deformed [4]. When the skeleton breaks the WC grains separate and slide. Sliding and separation between WC grains is believed to be one of the important factors behind the plastic deformation. The purpose of this thesis is therefore to investigate grain boundary sliding and separation in WC–Co. The stresses involved in grain boundary sliding and separation are to be found. In this thesis, clean boundaries between WC grains and grain boundaries with half a monolayer of Co are studied. The simulation method used is molecular dynamics using an analytical bond order potential. It will therefore be sufficient to use on the order of 10^5 atoms. Molecular dynamics simulations where the number of atoms are of higher order will be impractical due to computational cost. Periodic boundary conditions are used to model large grain boundaries. In figure 1.3 a typical system can be seen. Sliding and separation simulations are done by applying a constant strain rate to the system.
The results from this thesis can be adapted to grain boundary laws to be used can be used in mesoscopic finite element method simulations. These mesoscopic simulations are performed on systems with several grains.

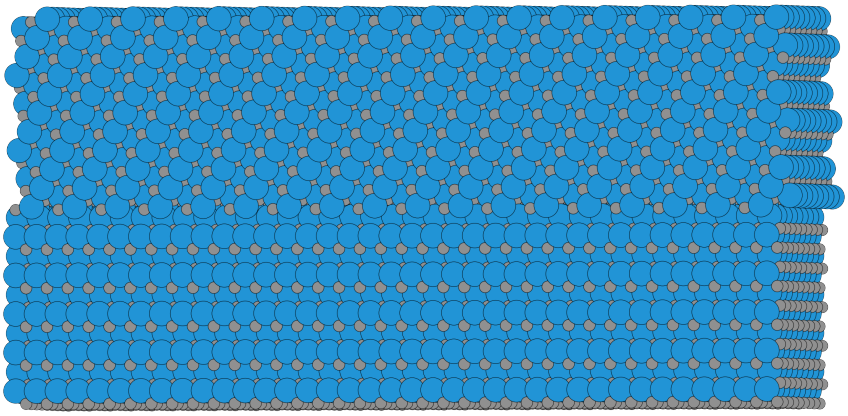

Figure 1.3: The figure represent a typical simulation system used in the MD simulations, where W is blue and C is grey. This specific grain boundary is a clean Σ4 WC/WC grain boundary with a W-II prismatic surface and a C-I $(\bar{1}012)$ surface.

2. Simulation Method

The simulation method used in this thesis is known as molecular dynamics (MD). MD is a computer simulation technique where the equations of motion are integrated to give the time evolution of a set of atoms or molecules [5]. MD follows the laws of classical mechanics which means that the acceleration of each atom is calculated from Newton's second law. This means that the time evolution will be completely determined from the initial positions and velocities of the atoms, which makes MD a deterministic technique. Only the precision of the floating point system and the discrete integration time step will make the simulation deviate from the analytical trajectory.
The classical mechanics approximation of the motion of the atoms and molecules is accurate [6]. Quantum effects are only relevant for light atoms or molecules, or for vibrational and rotational motion with high frequency.
An MD simulation follows a similar procedure as a real experiment [5]. First, a sample is prepared, i.e. a model system is chosen. Then the system is equilibrated so that the properties of the system no longer change with time. This is done by simply solving Newton's equations of motion. When the system is equilibrated the actual measurement can be performed.

2.1 Algorithms

In an MD simulation there are different methods of integrating Newton's equations of motion with different orders of the error [6]. The algorithm used in this thesis is the velocity Verlet algorithm. If the time step in the MD simulation is Δt then the evolution of the position is

$$r(t + \Delta t) = r(t) + v(t)\Delta t + \frac{f(t)}{2m}\Delta t^2 \tag{2.1}$$

where $f(t)$ is the force given by the interaction potential which is discussed in chapter 3. The velocity is calculated as

$$v(t + \Delta t) = v(t) + \frac{f(t + \Delta t) + f(t)}{2m}\Delta t. \tag{2.2}$$

The error in the position is of order $\mathcal{O}(\Delta t^4)$. In this work the time step used is chosen to be 1 fs.

2.2 Measuring observables

To measure an observable quantity in an MD simulation the observable must first be expressed using the positions, momenta, and forces of the particles in the system. In this work

the important observables are temperature, pressure, and stress. The Hamiltonian H for the system can be expressed as

$$H = \sum_i \frac{p_i^2}{2m_i} + U(\mathbf{r}_1,...,\mathbf{r}_N). \tag{2.3}$$

In the canonical ensemble for identical particles the partition function for fixed number of particles N, volume V and temperature T may be written as

$$\begin{aligned} Q_{NVT} &= \frac{1}{N!}\int \frac{\mathrm{d}^{3N}r\,\mathrm{d}^{3N}p}{h^{3N}} \exp\left[-\frac{H}{k_BT}\right] = \\ &= \underbrace{\frac{1}{N!}\int \frac{\mathrm{d}^{3N}p}{h^{3N}} \exp\left[-\frac{\sum_i \frac{p_i^2}{2m_i}}{k_BT}\right]}_{Q^{\mathrm{id}}_{NVT}} \underbrace{\int \mathrm{d}^{3N}r \exp\left[-\frac{U(\mathbf{r}_1,...,\mathbf{r}_N)}{k_BT}\right]}_{Q^{\mathrm{ex}}_{NVT}} \end{aligned} \tag{2.4}$$

Here the partition function has been divided into an kinetic (ideal gas) part Q^{id}_{NVT} and a potential (excess) part Q^{ex}_{NVT} [7].

2.2.1 Temperature

To measure the temperature it is convenient to use the equipartition of energy over all degrees of freedom that enter quadratically in the Hamiltonian of the system [8]. The equipartition of the kinetic energy is derived from the expectation value of the kinetic energy E_{kin}

$$\langle E_{\mathrm{kin}}\rangle = \left\langle \sum_i \frac{p_i^2}{2m_i} \right\rangle = \frac{\int \sum_i \frac{p_i^2}{2m_i} \exp\left[-\frac{\sum_i \frac{p_i^2}{2m_i} + U(\mathbf{r}_1,...,\mathbf{r}_N)}{k_BT}\right] \mathrm{d}^{3N}p\,\mathrm{d}^{3N}r}{\int \exp\left[-\frac{\sum_i \frac{p_i^2}{2m_i} + U(\mathbf{r}_1,...,\mathbf{r}_N)}{k_BT}\right] \mathrm{d}^{3N}p\,\mathrm{d}^{3N}r}, \tag{2.5}$$

where i is taken over all particles and the integrals are taken over all positions and momenta. Here the integrals over the positions cancel and the integral over each of the three momentum dimensions will be equal. Integrals over the particles is also identical. The expectation of the kinetic energy can therefore be simplified and expressed as

$$\langle E_{\mathrm{kin}}\rangle = 3N\frac{\int \frac{p^2}{2m} \exp\left[-\frac{p^2}{2mk_BT}\right] \mathrm{d}p}{\int \exp\left[-\frac{p^2}{2mk_BT}\right] \mathrm{d}p} = \frac{3Nk_BT}{2}. \tag{2.6}$$

This means that the kinetic energy of each degree of freedom is $\frac{k_BT}{2}$ and the temperature can be expressed as

$$T = \frac{2\langle E_{\mathrm{kin}}\rangle}{3Nk_B}. \tag{2.7}$$

In MD simulations the total momentum is often set to zero which means that there are 3 less degrees of freedom. The temperature is then given by

$$T = \frac{2\langle E_{\mathrm{kin}}\rangle}{3(N-1)k_B}. \tag{2.8}$$

2.2.2 Pressure

The pressure is more difficult to measure than the temperature. The most common way is based on the virial equation for the pressure [8]. From thermodynamics the pressure at constant temperature and with constant number of particles can be written as

$$P = k_B T \frac{1}{Q^{ex}_{NVT}} \frac{\partial Q^{ex}_{NVT}}{\partial V}, \tag{2.9}$$

To calculate the volume dependence of Q^{ex}_{NVT} it is convenient to work in dimensionless coordinates

$$\mathbf{r}_i = V^{\frac{1}{3}} \mathbf{s}_i. \tag{2.10}$$

Then Q^{ex}_{NVT} from equation (2.4) may be written as

$$Q^{ex}_{NVT} = V^N \int \exp\left[-\frac{U\left(V^{\frac{1}{3}}\mathbf{s}_1,...,V^{\frac{1}{3}}\mathbf{s}_N\right)}{k_B T} \right] \mathrm{d}^{3N} s. \tag{2.11}$$

Derivation with respect to V gives

$$\frac{\partial Q^{ex}_{NVT}}{\partial V} = \frac{N Q^{ex}_{NVT}}{V} - \frac{V^{N-\frac{2}{3}}}{3 k_B T} \int \sum_i \mathbf{s}_i \nabla_i U \exp\left[-\frac{U\left(V^{\frac{1}{3}}\mathbf{s}_1,...,V^{\frac{1}{3}}\mathbf{s}_N\right)}{k_B T} \right] \mathrm{d}^{3N} s. \tag{2.12}$$

Combining this with equation (2.9) and using the definition of expectation values gives

$$P = \frac{N k_B T}{V} - \frac{1}{3V} \left\langle \sum_i \mathbf{r}_i \frac{\partial U}{\partial \mathbf{r}_i} \right\rangle. \tag{2.13}$$

This is the virial theorem for pressure.

2.2.3 Stress

The pressure expression can be generalized to give the expression for the stress tensor

$$\sigma_{\alpha\beta} = -\frac{1}{V} \sum_i \left\langle \frac{p_i^\alpha p_i^\beta}{m_i} - \frac{\partial U}{\partial r_i^\alpha} r_i^\beta \right\rangle, \tag{2.14}$$

where α and β refer to the directions x, y, or z [9]. From this it is trivial to show that

$$P = -\frac{\sigma_{xx} + \sigma_{yy} + \sigma_{zz}}{3}, \tag{2.15}$$

i.e. one third of the trace of the stress is equal to the negative pressure.

2.3 Controlling observables

Methods of controlling the values of observables such as temperature and pressure [6], i.e. a thermostat and a barostat, are needed in order to equilibrate the system. First, consider the temperature of the system. From equation (2.8) it is straightforward to see that controlling the velocities of the particles will have the effect of controlling the temperature of the system. However, rescaling the velocities will only give ensembles that have the correct averages for properties that only depend on the positions of the particles. Better methods are needed.
A popular thermostat is the Nosé-Hoover thermostat. The main idea is to add additional coordinates to the Lagrangian of the system which will act as fictive particles which interacts with the other particles. To control the temperature these additional coordinates are coupled to the particles velocities. This is the thermostat used in the thesis.
Now consider the pressure of the system. By modifying the volume of the system the pressure will change. This can be seen in equation (2.13). One way to control the pressure is to use the same method as for the temperature but let the additional parameters be coupled to the positions of the particles of the system. This is called a Nosé-Hoover barostat and it is the barostat used in this thesis.

2.4 Performing simulations

The MD simulations are performed using LAMMPS (Large-scale Atomic/Molecular Massively Parallel Simulator) [10]. Periodic simulation cells have been used in the LAMMPS simulations. However, only periodicity in the directions parallel to the grain boundary plane is wanted in the simulations. To make the whole system respect the periodic boundary conditions the system is ended with free surfaces on both sides with added vacuum. This prevents interaction across the boundaries of the periodic simulation cell in the direction perpendicular to the grain boundary plane.
The sliding and separation simulations were performed by exposing the grain boundary systems to a constant strain rate. First the system is minimized with respect to energy using the conjugate gradient method. After that, it is equilibrated to the desired pressure and temperature using the thermostat and barostat described earlier. Next, a thin region at the free surface of one of the grains is fixed in the direction of sliding or separation. A constant velocity is then applied to a thin region at the free surface of the other grain. The two slabs will then start to move with respect to each other, i.e. they will start to slide or separate. The region between the two regions at the free surfaces are only exposed to a thermostat to keep the temperature correct during the simulations.
The tensile or compressive stress is created by adding a force on the particles in the region that is being moved. To give the C and W atoms the same acceleration the added force is set proportional to the mass of C and W.
Since it is unclear how individual atoms will move and behave near the grain boundary it is not possible to directly measure the displacement or separation in the grain boundary by measuring the grain boundary atoms. Instead, the motion in the grain boundary can be monitored by having several marker regions in each slab whose center of mass is measured. Both slabs will deform elastically and translate. By measuring the center of mass of the marker region the elastic and translating parts can be separated. It is then possible to

extrapolate the motion of each grain down to the grain boundary. This is schematically shown for sliding grains in figure 2.1. Since the grains deform elastically the motion for example along the grain boundary will be influenced by the deformation perpendicular to the grain boundary. As the size of the grain perpendicular to the grain boundary change, the extrapolation of the motion along the grain boundary must change. The relative displacement between the marker regions is therefore monitored in all directions for both sliding and separation. These are then combined to estimate the motion between the grains. Since the purpose is to find stresses under sliding and separation the most interesting data from the simulations will be the stress, shear stress σ_{xz} for sliding and normal stress σ_{zz} for separation, as a function of the displacement in the grain boundary. For separation it will be the displacement perpendicular to the grain boundary and for sliding the displacement parallel to the grain boundary. There are two important parts of these results. First, the peak value of the stress is identified as the critical stress needed for sliding or separation to occur at the given strain rate. Second, there is the plateau value of the stress when the sliding has started which will be dominated by viscous forces. These two values can be viewed as static friction and dynamic friction. A schematic figure of the results from a sliding simulation can be seen in figure 2.2. For a separation simulation the graph will be quite similar with a plateau stress of 0.

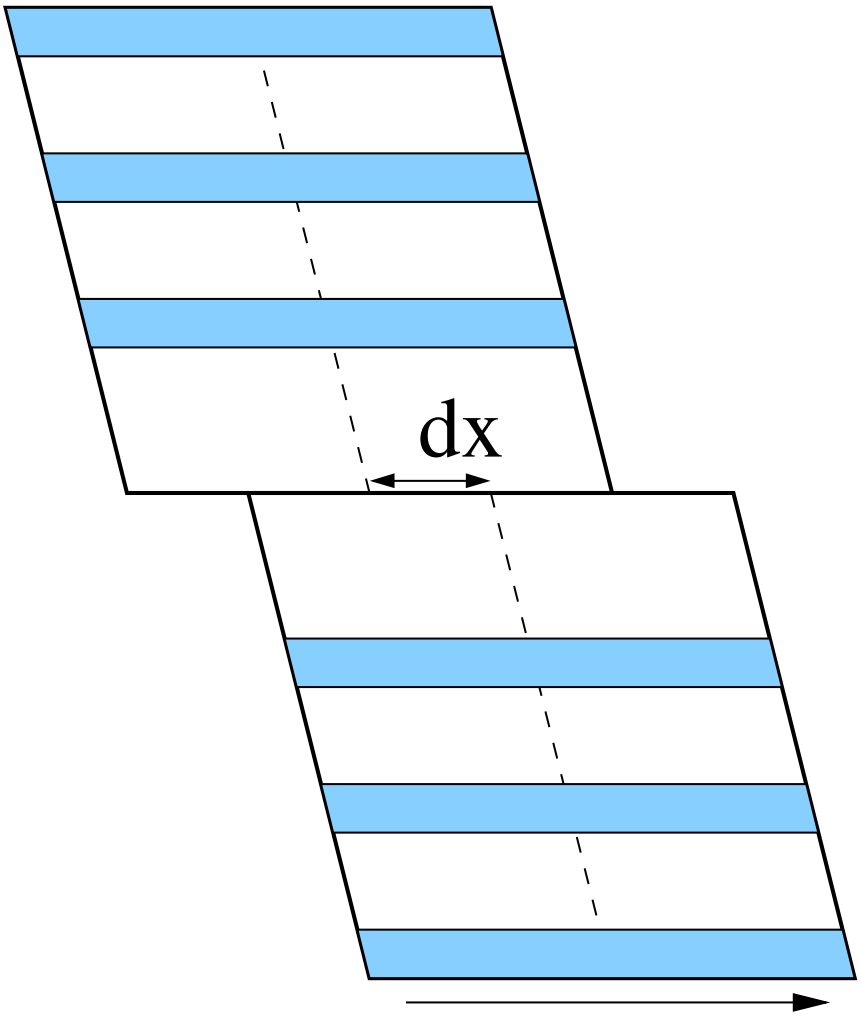

Figure 2.1: Image of how the extrapolation is performed using several marker regions (shaded blue) in each slab.

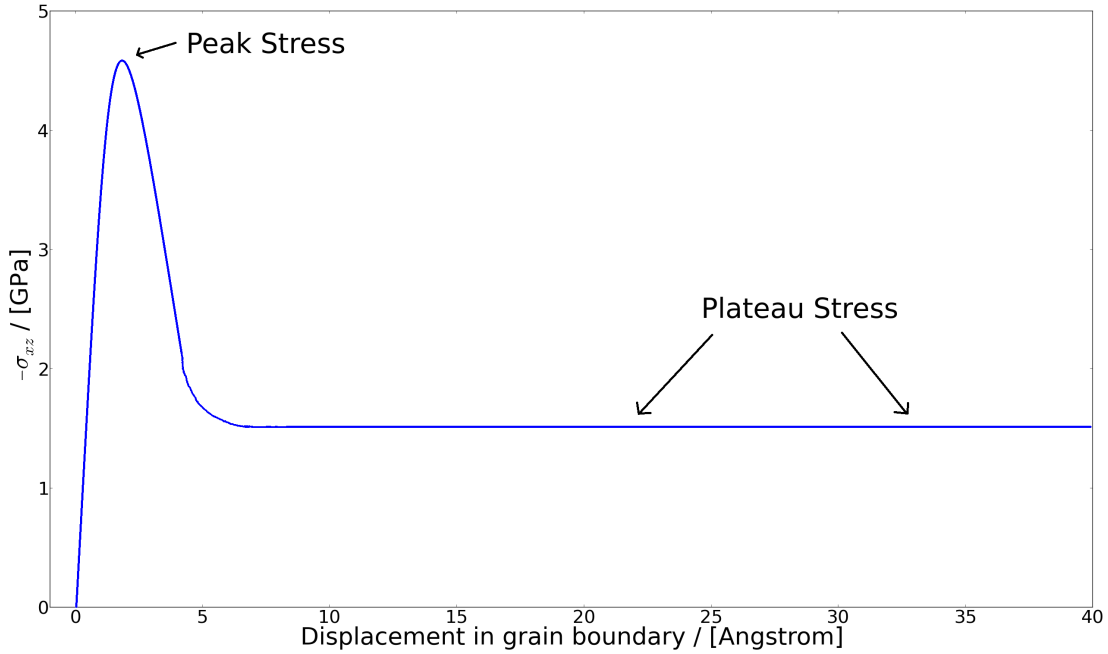

Figure 2.2: Schematic plot of the stress versus the displacement in the grain boundary.

3. Interaction Potential

The potential used in the simulations is a Tersoff type potential, which is an analytical bond order potential (ABOP) [11, 12]. The Tersoff potential is a three body potential. The total energy of a system is computed as

$$E = \frac{1}{2}\sum_{i \neq j} V_{ij}, \tag{3.1}$$

where the sums are taken over all particles. The Tersoff potential is written as

$$V_{ij} = f_C(r_{ij})\left[f_R(r_{ij}) + b_{ij} f_A(r_{ij})\right], \tag{3.2}$$

where $f_C(r_{ij})$ is a cut-off function given by

$$f_C(r_{ij}) = \begin{cases} 1 & : \quad r < R - D \\ \frac{1}{2} - \frac{1}{2}\sin\left(\frac{\pi}{2}\frac{r-R}{D}\right) & : \quad R - D < r < R + D \\ 0 & : \quad r > R + D \end{cases}. \tag{3.3}$$

This appears to be a pair potential, but the bond-order parameter b_{ij} can be constructed to give contribution from triplets of atoms. R and D are chosen to only include the first neighbour-shell. $f_R(r_{ij})$ and $f_A(r_{ij})$ are the repulsive and attractive part of the potential respectively. They are given by

$$f_R(r_{ij}) = Ae^{-\lambda_1 r} \tag{3.4}$$

$$f_A(r_{ij}) = -Be^{-\lambda_2 r}. \tag{3.5}$$

b_{ij} is given by

$$b_{ij} = \left(1 + \beta^n \zeta_{ij}^n\right)^{-\frac{1}{2n}}, \tag{3.6}$$

where

$$\zeta_{ij} = \sum_{k \neq i,j} f_C(r_{ik}) g(\theta_{ijk}) e^{\lambda_3^m (r_{ij} - r_{ik})^m}, \tag{3.7}$$

where θ_{ijk} is the bond angle between bonds ij and ik. This makes the potential a three body potential. The function $g(\theta)$ is given by

$$g(\theta) = \gamma\left(1 + \frac{c^2}{d^2} - \frac{c^2}{d^2 + (\cos\theta - \cos\theta_0)^2}\right) \tag{3.8}$$

All parameters in the potential need to be fitted to more precise electron structure calculations. Tersoff potentials have been fitted for the WC and WC–Co systems [13, 14].

4. Simulation Systems

The system to be studied is WC–Co. The cemented carbide WC–Co consists of grains of WC embedded in an interconnected system of Co [1] [2]. In this thesis clean WC/WC grain boundaries and WC/WC grain boundaries with half a monolayer of Co will be studied. The WC lattice structure will first be introduced and then WC/WC grain boundaries will be explained. After that Co will be introduced in the system.

4.1 WC structure

WC has a simple hexagonal lattice with a 2-atom basis and space group $P\bar{6}$m2. It can be thought of as alternating hexagonally close packed layers of W and C. The lattice parameters are $a = 2.906\,\text{Å}$ and $c = 2.837\,\text{Å}$, where a is the lattice parameter in the hexagonal plane and c is the lattice parameter perpendicular to the hexagonal plane [16]. The structure can be seen in figure 4.1. Planes in the hexagonal lattice is described by four Miller-Bravais indices $(ijkl)$, where i and j are the indices for the two lattice basis vectors in the hexagonal plane separated by an angle $\frac{2\pi}{3}$. The third index is defined by $k = -i - j$, i.e. it is the index for a basis vector given as minus the sum of the other two basis vectors in the hexagonal plane. By doing so any permutation of i, j and k will describe planes with the same geometry in the hexagonal plane. l is the index for the lattice basis vector perpendicular to the hexagonal plane. The indices are given as the inverse intercepts along the lattice vectors. The Miller indices for the normal to the plane $(ijkl)$ is given as $[i,j,k,l\frac{3}{2}\left(\frac{a}{c}\right)^2]$.
Two important planes or surfaces in the WC crystal are the basal and prismatic planes. A basal plane has Miller indices (0001) and prismatic plane has miller indices $(\bar{1}010)$. Both of these can be seen in figure 4.2. The basal plane is the top of the hexagon and the prismatic plane is the side of the hexagon. A plane or surface is also specified by the termination of W or C. Since WC is two alternating close packed hexagonal layers of W and C there are two types of prismatic surfaces. This can be understood by looking at figure 4.3. The surface which has the second layer, i.e. the layer next after the terminating layer, close to the surface is called type I. The other surface which has the second layer farther away from the surface is called type II. Surfaces will therefore be specified by their termination and type. For example C-II means a carbon terminated surface of type II. Since there are alternating layers of W and C a C-II surface will have the same surface normal as a W-I surface. By switching both termination and type the orientation is preserved.

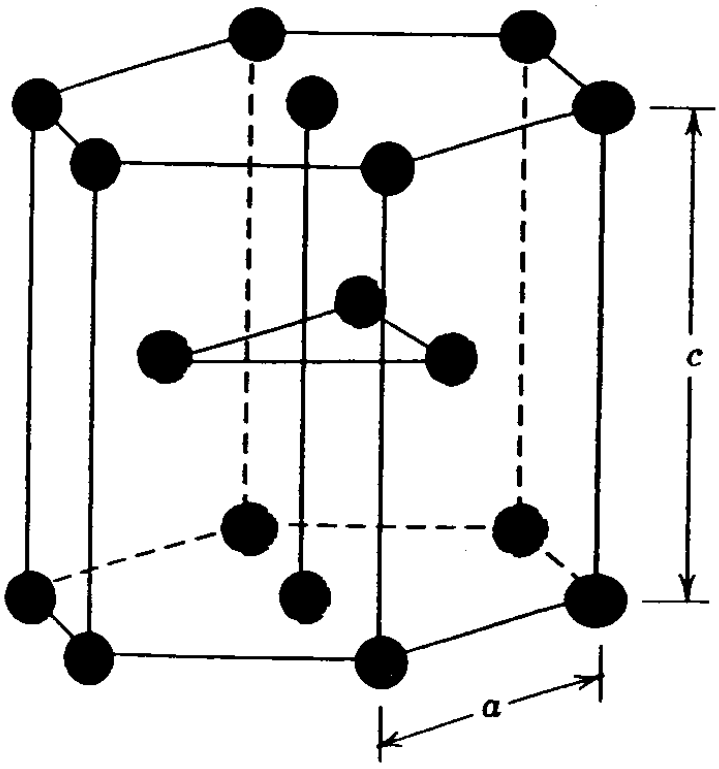

Figure 4.1: Simple hexagonal structure with WC basis [15].

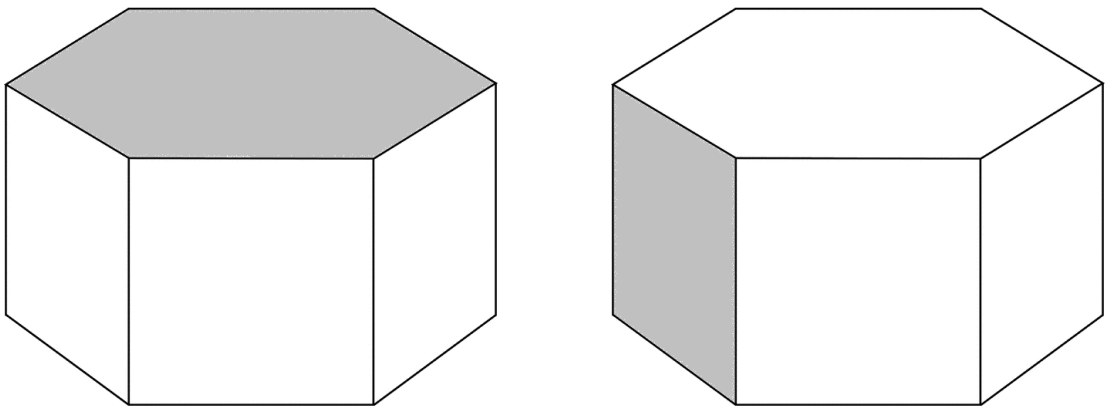

Figure 4.2: Basal surface (left) and prismatic surface (right).

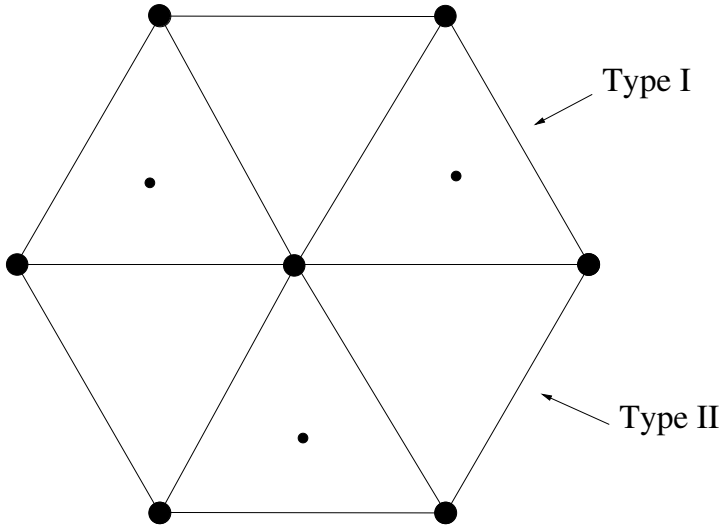

Figure 4.3: Description of the types of prismatic surfaces.

4.2 WC/WC grain boundaries

By letting $a = c$, it is possible to classify the grain boundaries between WC grains in terms of the coincidence index [17]. If a lattice is rotated around one lattice point there will be certain angles at which the rotated lattice will match the non-rotated lattice in a certain fraction of lattice points. The inverse of this fraction is the coincidence index. The coincidence index is denoted by Σ followed the index. For example if you rotate a square lattice $\frac{\pi}{2}$ it will match perfectly, i.e. a coincidence of $\Sigma 1$. If the lattice instead is rotated an angle $\arctan 0.75 \approx 0.64$ only one fifth of the lattice sites will coincide, i.e. a coincidence of $\Sigma 5$. The coincidence index of a grain boundary is defined as the the coincidence index of the lattices of the two grains that make up the grain boundary. In this thesis $\Sigma 4$ grain boundaries will be studied. A $\Sigma 4$ coincidence index can be created by rotating the WC crystal $\frac{\pi}{3}$ around the $[1\bar{2}10]$ axis. A $\Sigma 4$ can then be made by joining a rotated and an non-rotated grain. The surfaces in the grain boundary are arbitrary as long as the relative orientation of the grains is kept at the $\Sigma 4$ coincidence. Experiments have shown that about 60% of grain boundaries in WC contain at least one basal or one prismatic plane [18]. $\Sigma 4$ grain boundaries built up of one prismatic surface have been chosen to be studied in this thesis. By choosing one of the surfaces to be prismatic the other surface will be $(\bar{1}012)$.In figure 4.1 a $\Sigma 4$ grain boundary can be seen. There will be two types of $(\bar{1}012)$ surfaces just like the two types of prismatic surfaces. Again, type I will be associated to the surface where the second atom layer lies closer to the terminating layer. Type II will have its second atom layer farther away from the terminating layer. Just like for the prismatic surfaces the $(\bar{1}012)$ surfaces are specified by their termination and type. The two pairs of termination and type: (W-I,C-II) and (W-II,C-I) each have the same surface normal. If a grain is rotated π around the $[1\bar{2}10]$ axis the surface will switch from one of the pairs to the other pair. Since both grains in the grain boundary can be rotated, there are four versions of the $\Sigma 4$ coming from the orientation of the grains. These four will be called $\Sigma 4.1$, $\Sigma 4.2$, $\Sigma 4.3$ and $\Sigma 4.4$.

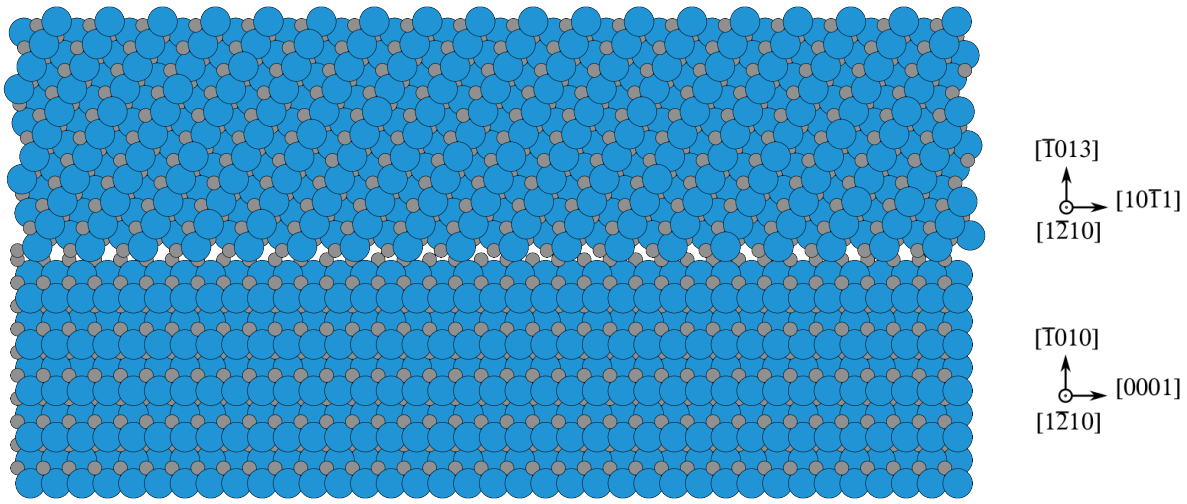

Figure 4.4: $\Sigma 4$ grain boundary seen in the $(1\bar{2}10)$ plane. This includes one repeating unit in the direction of misfit. W (blue) and C (grey).

The easiest way to see which of the four $\Sigma 4$ a specific grain boundary belongs to is to look at the terminations and types of the surfaces in the grain boundary. Here it is useful to use the fact that surfaces with different termination and type will have the same orientation. The prismatic and $(\bar{1}012)$ surfaces are distinguished. In table 4.1 there is a list of which terminations that are associated to which grain boundary. These will be the grain boundaries studied in this thesis. There is a total of 16 clean grain boundaries.
When $a \neq c$ then the angle to cut will change to $\arctan\left(\frac{\sqrt{3}a}{c}\right)$ and there will be a mismatch in size between the two slabs. The mismatch is in the direction perpendicular to the hexagonal plane for the slab with the prismatic surface. When simulations are performed it is therefore desirable to have a big enough system to get a repeating structure. The length of the repeating unit of the $(\bar{1}012)$ surface is $d = \sqrt{3a^2 + c^2}$ and c for the $(\bar{1}010)$ surface. To make one repeating cell, integers M,N such that $Md \approx Nc$ has to be found. The equilibrium lattice constants of the ABOP are $a = 2.9166\,\text{Å}$ and $c = 2.8121\,\text{Å}$. Using the equilibrium lattice constants of the ABOP and $M = 18$ and $N = 37$ gives an error of only $Md - Nc \approx 0.022\,\text{Å}$. This means a relative error of $\frac{Md-Nc}{Nc} \approx 0.00021$. The system will thus have a repeating cell of $37c$ in the direction of the misfit. In figure 4.4 one repeating unit is shown. In simulations the direction of misfit is aligned with the x-direction, the direction of perfect match is aligned with the y-direction and the direction perpendicular to the grain boundary is thus aligned with the z-direction.

4.3 Grain boundaries with half a monolayer of Co

In order to introduce Co in the the grain boundaries, W or C atoms are replaced by Co. To get half a monolayer every other atom in a monolayer is substituted. 3 possible sites in the

	Surfaces	
Grain boundary	$(\bar{1}010)$	$(\bar{1}012)$
Σ4.1	C-I	C-II
	C-I	W-I
	W-II	C-II
	W-II	W-I
Σ4.2	C-I	C-I
	C-I	W-II
	W-II	C-I
	W-II	W-II
Σ4.3	C-II	C-II
	C-II	W-I
	W-I	C-II
	W-I	W-I
Σ4.4	C-II	C-I
	C-II	W-II
	W-I	C-I
	W-I	W-II

Table 4.1: Table of which terminations are connected to which grain boundary.

grain boundary to substitute with cobalt to give half a monolayer are considered in this thesis. First, the outmost layer in the prismatic surface. This will be called site 1. Second, the outer layer in the $(\bar{1}012)$ surface which will be called site 2. Third, the second outmost layer of the $(\bar{1}012)$ surface which will be called site 3. There are thus 48 different grain boundariey configurations with segregated cobalt to be considered. The sites are shown in figure 4.5.

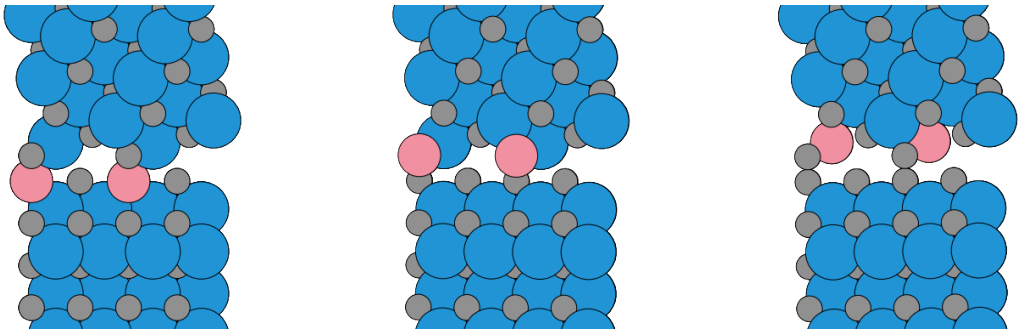

Figure 4.5: The different sites for cobalt replacement. site 1 (left), site 2 (middle) and site 3 (right). W (blue), C (grey) and Co (pink).

5. Results

Before doing MD simulations it is interesting to see how well the interaction potential describes grain boundaries in the WC and WC–Co system. The accuracy is compared with Density Functional Theory (DFT) calculations [19]. DFT calculations deals more precisely with quantum mechanical effects [20]. Only one of the 16 possible clean $\Sigma 4$ grain boundaries and one of the possible 48 segregated grain boundaries will be used in the separation and sliding calculations. It is desirable to do these simulations with the most stable grain boundary, i.e. the one which has the lowest energy, as this grain boundary is most representative. When a $\Sigma 4$ grain boundary system is created, two free surfaces are also created as described in chapter 2. There will be one prismatic surface and one $(\bar{1}012)$ surface. This means that these two surfaces will contribute to the energy of the system. To be able to find out the grain boundary energy the energies of the free surfaces must first be known. In this part the systems are only minimized with respect to energy using the conjugate gradient method.

5.1 Surface energies

The geometry of the WC crystal can be used to calculate the surface energies [2]. There are 6 prismatic surfaces surrounding the WC hexagon, 3 of each type. It is therefore possible to make an equilateral triangle with three prismatic surfaces of the same type. Such a triangle is shown in figure 5.1. By having periodic boundary conditions in the direction perpendicular to the hexagonal plane there will only be one type of surface in the system. However, not only will the surfaces affect the energy of the system, the edges will as well. To avoid edge atoms moving away from the triangles under energy minimization they are removed. This makes the edges of the triangles less sharp. To cancel the effects from the edges several triangles with different sizes are made. An extrapolation to an infinite triangle makes it possible to calculate the value of the surface energy.
The excess free energy from the surfaces and edges ΔG is approximated as the excess total energy ΔE given by

$$\Delta E = E_{\text{tot}} - N_{\text{C}}\mu_{\text{C}} - N_{\text{W}}\mu_{\text{W}}, \tag{5.1}$$

where E_{tot} is the total energy of the triangle, N_{C} the number of carbon atoms and N_{W} the number of tungsten atoms. μ_{W} and μ_{C} are the chemical potentials of single tungsten and carbon atoms. The chemical potential for a WC unit is the sum of the chemical potentials for single atoms,

$$\mu_{\text{WC}} = \mu_{\text{W}} + \mu_{\text{C}}. \tag{5.2}$$

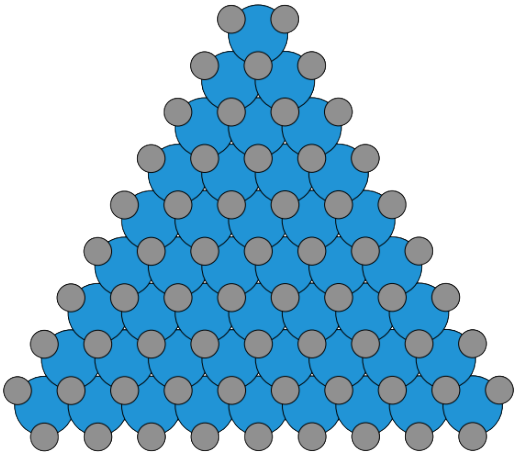

Figure 5.1: Equilateral triangle with C-II terminated prismatic surfaces. W (blue) and C (grey).

Equation (5.1) may then be rewritten as

$$\Delta E = E_{\text{tot}} - N_{\text{W}}\mu_{\text{WC}} - (N_{\text{C}} - N_{\text{W}})\,\mu_{\text{C}}, \tag{5.3}$$

The chemical potential for a WC unit can be found by relaxing a bulk WC system using the interaction potential and dividing the total energy by half the number of atoms. The chemical potential for C must then be chosen. In this thesis the two phase WC–Co system is modelled. A two phase WC–Co sample is stable in a narrow range of C content in the sample. Outside this range of C content there will be additional or other phases present. If the content of C is increased there will also be C in graphite phase in the sample and if the content of C is lowered there will instead be C in η phase. There are therefore two limits for the chemical potential of C: graphite and η. In this thesis the graphite limit is used.
The excess energy can be divided into two parts, one from the surfaces and one from the edges. This can be expressed as

$$\Delta E = 3Ld\sigma + 3d\delta, \tag{5.4}$$

where L is the side length of the triangle, d is the height of the triangle, σ is the surface energy and δ is the edge energy. Dividing by $3Ld$ which is the area of the triangle gives

$$\frac{\Delta E}{3Ld} = \sigma + \frac{\delta}{L}. \tag{5.5}$$

Making a linear fit of $\frac{\Delta E}{3Ld}$ against $\frac{1}{L}$ will thus result in a line with slope δ and y-intercept σ. A graph showing the extrapolation of the excess energy for one prismatic surface can bee seen in figure 5.3.
Calculating the surface energies for the $(\bar{1}012)$ surfaces is less simple. It is not possible to make a triangle with 3 identical $(\bar{1}012)$ surfaces, however, isosceles triangles with two identical $(\bar{1}012)$ surfaces and one prismatic surface can be made. Such a triangle can be seen in figure

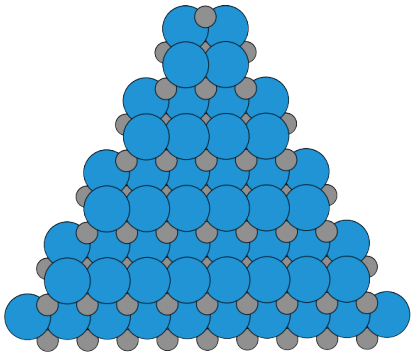

Figure 5.2: Isosceles triangle with two W-II ($\bar{1}012$) surfaces and one C-I prismatic surface. W (blue) and C (grey).

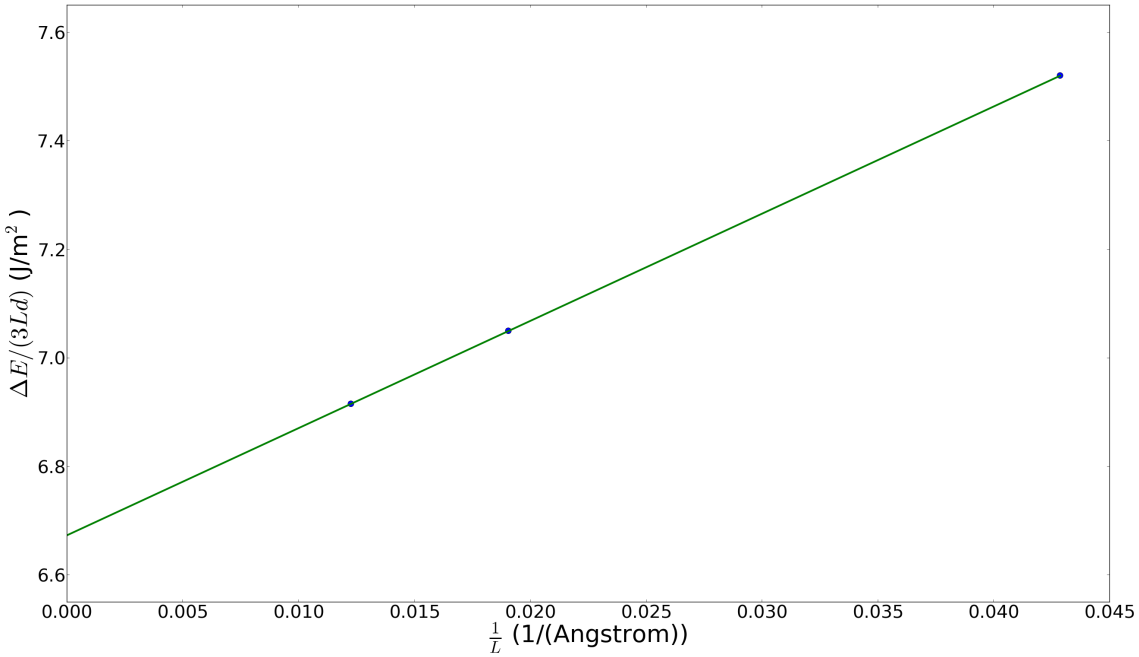

Figure 5.3: Graph showing the extrapolation to infinite length of equilateral triangles with C-II prismatic surfaces.

Surface	Surface Energy (J/m^2)
C-I	2.77
C-II	6.67
W-I	1.81
W-II	3.65

Table 5.1: Prismatic surface energies (J/m^2)

Surface	Surface Energy (J/m^2)
C-I	4.08
C-II	4.17
W-I	3.23
W-II	2.99

Table 5.2: ($\bar{1}012$) surface energies (J/m^2)

5.2. The value of the prismatic surface energy will be known from previous calculations and it can thus be eliminated so that the ($\bar{1}012$) surface energy can be found. Since this triangle is isosceles it will have two edges that are identical and one that is different from the other two. It will also have two sides of equal length L, and one with different length L'. The excess energy may then be expressed as

$$\Delta E = 2Ld\sigma + L'd\sigma' + 2d\delta + d\delta', \tag{5.6}$$

where σ is the surface energy for the ($\bar{1}012$) surface, σ' the surface energy for the prismatic surface, δ the edge energy for the edges between the prismatic surface and the other two surfaces and δ' the edge energy for the edge between the two ($\bar{1}012$) surfaces. The equation for the excess energy can be rewritten as

$$\frac{\Delta E}{2Ld} = \sigma + \frac{L'\sigma'}{2L} + \frac{2\delta + \delta'}{2L}. \tag{5.7}$$

$\frac{L'\sigma'}{2L}$ is a constant that is known from previous calculations and from the geometry of the triangles. Like above a linear fit of $\frac{\Delta E}{2Ld} - \frac{L'\sigma'}{2L}$ against $\frac{1}{L}$ will give a line with descent $\frac{2\delta+\delta'}{2}$ and y-intercept σ.
Surface energies were calculated for both tungsten and carbon terminated surfaces, for both type 1 and 2 and for both the prismatic and ($\bar{1}012$) surfaces i.e. a total of 8 surface energies. The values of the surface energy density can be found in tables 5.1 and 5.2.

5.2 Grain boundary and segregation energies

The grain boundary energies for all 64 $\Sigma 4$ grain boundary configurations will be calculated. DFT calculations are computationally costly and the calculations are therefore done in the $a = c$ approximation which will give no mismatch and smaller systems can therefore be used. The MD calculations must be done in the same way. However, using the $a = c$ approximation

creates a new problem. When the two slabs are strained to $a = c$ the bulk energy for a WC unit, E_{WC}, in the two slabs will shift. Therefore, a value of $a = c$ must be found which gives equal bulk energies in the two slabs. This is done by calculating the bulk energies for the two slabs separately for many values of $a = c$ and plotting the values together. The value for $a = c$ is found as the point where the two curves intersect. To mimic the constraints in the grain boundary calculations the bulk energies are calculated using slabs with two free surfaces. The total energy is found for two different slabs with different number of layers perpendicular to the grain boundary and the difference of these divided by half of the difference in number of atoms gives the bulk energy. For the ABOP the lattice parameter became $a = c = 2.8632\,\text{Å}$.
In attempt to optimize the grain boundary energy with respect to translation in the the grain boundary plane some different initial translations is applied before the energy minimization. For clean grain boundaries and cobalt in site 1 four high symmetry translations have been used: (0,0,0), ($\frac{a}{2}$,0,0), (0,$\frac{a}{2}$,0) and ($\frac{a}{2}$,$\frac{a}{2}$,0). These are given in Cartesian coordinates and should not be confused with the Miller indeces. The orientation of the grain boundary in Cartesian coordinates is explained in chapter 4. For cobalt in site 2 and site 3 eight high symmetry translations have been used: (0,0,0), ($\frac{a}{2}$,0,0), (a,0,0), ($\frac{3a}{2}$,0,0), (0,$\frac{a}{2}$,0), ($\frac{a}{2}$,$\frac{a}{2}$,0), (a,$\frac{a}{2}$,0) and ($\frac{3a}{2}$,$\frac{a}{2}$,0).
The grain boundary energy is calculated as

$$E_{\text{grain boundary}} = \frac{E_{\text{tot}} - N_{\mathrm{C}}\mu_{\mathrm{C}} - N_{\mathrm{W}}\mu_{\mathrm{W}} - N_{\mathrm{Co}}\mu_{\mathrm{Co}}}{A} - \sigma_{\text{tot}}, \tag{5.8}$$

where A is the area of the grain boundary and σ_{tot} is the sum of the surface energies for the two free surfaces. This can be rewritten as

$$E_{\text{grain boundary}} = \frac{E_{\text{tot}} - N_{\mathrm{W}}\mu_{\mathrm{WC}} - (N_{\mathrm{C}} - N_{\mathrm{W}})\,\mu_{\mathrm{C}} - N_{\mathrm{Co}}\mu_{\mathrm{Co}}}{A} - \sigma_{\text{tot}}. \tag{5.9}$$

The value for the chemical potential of cobalt μ_{Co} is taken from bulk calculation of Co in a hexagonal close-packed lattice using the ABOP. The segregation energy is the difference between the energy for a grain boundary with and without segregated cobalt.
The resulting energies can be found in tables 5.3 and 5.4. The tables includes the results from both ABOP and DFT calculations. Table 5.3 includes energies for grain boundaries with segregated cobalt for all sites. Table 5.4 includes the clean grain boundary energies as well as the energies for grain boundaries with cobalt in the optimal site. It also includes segregation energies.
In figure 5.4 there is a plot of the grain boundary energies from DFT against the values from ABOP. The data shows that the ABOP potential shows the same trends as DFT. However, the two methods do not give the same most stable grain boundary. The DFT results are believed to be more reliable and the grain boundaries with the lowest energies from DFT calculations will therefore be chosen. This means that the most stable clean grain boundary is the $\Sigma 4$ with a tungsten terminated prismatic surface of type II and carbon terminated $(\bar{1}012)$ surface of type I. The most stable grain boundary with half a monolayer cobalt is the $\Sigma 4$ with a carbon terminated prismatic surface of type I and carbon terminated $(\bar{1}012)$ surface of type I and with cobalt lying in site 1, i.e. in the outer layer of the prismatic surface. In both cases it is the $\Sigma 4.2$ grain boundary that is most stable.
In figure 5.5 there is a plot comparing the segregation energies from DFT and ABOP calculations. ABOP and DFT show the same trend and the results clearly show that Co will segregate.

	Surfaces		site 1		site 2		site 1	
Grain Boundary	$(\bar{1}010)$	$(\bar{1}012)$	ABOP	DFT	ABOP	DFT	ABOP	DFT
Σ4.1	C-I	C-II	**2.62**	**2.52**	4.09	2.98	4.76	4.81
	C-I	W-I	2.80	2.72	2.75	**2.35**	**2.63**	2.61
	W-II	C-II	3.68	**3.18**	4.58	3.29	**3.17**	3.37
	W-II	W-I	2.60	**2.65**	**2.54**	2.77	3.43	2.80
Σ4.2	C-I	C-I	**2.00**	**1.52**	2.32	1.89	4.16	3.73
	C-I	W-II	**2.42**	**2.66**	4.26	2.74	3.28	3.31
	W-II	C-I	2.20	1.96	3.34	2.76	**1.97**	**1.59**
	W-II	W-II	3.14	3.26	**2.81**	**3.10**	4.43	5.24
Σ4.3	C-II	C-II	**4.12**	**3.37**	4.13	4.31	7.93	5.56
	C-II	W-I	**2.73**	2.73	5.21	4.24	3.93	**1.94**
	W-I	C-II	3.47	3.34	3.91	**2.92**	**2.53**	3.63
	W-I	W-I	2.37	1.95	**1.86**	**1.70**	3.00	2.33
Σ4.4	C-II	C-I	**3.47**	**3.38**	4.27	3.45	6.80	5.24
	C-II	W-II	**3.21**	**3.15**	4.87	3.39	4.73	4.30
	W-I	C-I	3.38	3.11	2.94	**2.03**	**2.41**	2.39
	W-I	W-II	3.06	2.89	**2.41**	**2.48**	3.46	3.73

Table 5.3: Energies for grain boundaries (J/m^2) with segregated cobalt for different sites using ABOP and DFT. The optimal sites are highlighted in bold.

Surfaces		Clean		Cobalt				Segregation Energy	
$(\bar{1}010)$	$(\bar{1}012)$	ABOP	DFT	ABOP	site	DFT	site	ABOP	DFT
C-I	C-II	3.70	3.83	2.62	1	2.52	1	−1.08	−1.31
C-I	W-I	**2.81**	**3.24**	2.63	3	**2.35**	2	−0.18	−0.89
W-II	C-II	3.30	4.08	3.17	3	3.18	1	−0.13	−0.90
W-II	W-I	3.18	3.55	**2.54**	2	2.65	1	−0.64	−0.90
C-I	C-I	3.09	2.95	2.00	1	**1.52**	1	−1.09	−1.43
C-I	W-II	**2.56**	3.31	2.42	1	2.66	1	−0.14	−0.65
W-II	C-I	2.78	**2.09**	**1.97**	3	1.59	3	−0.81	−0.50
W-II	W-II	3.55	3.88	2.81	2	3.10	2	−0.74	−0.78
C-II	C-II	7.83	5.56	4.12	1	3.37	1	−3.71	−2.19
C-II	W-I	3.37	3.33	2.73	1	1.94	3	−0.64	−1.39
W-I	C-II	**2.50**	3.53	2.53	3	2.92	2	0.03	−0.61
W-I	W-I	2.76	**2.16**	**1.86**	2	**1.70**	2	−0.90	−0.46
C-II	C-I	6.02	4.80	3.47	1	3.38	1	−2.55	−1.42
C-II	W-II	3.32	3.20	3.21	1	3.15	1	−0.11	−0.05
W-I	C-I	**2.62**	**2.65**	**2.41**	3	**2.03**	2	−0.21	−0.62
W-I	W-II	3.04	2.69	**2.41**	2	2.48	2	−0.63	−0.21

Table 5.4: Energies for grain boundaries (J/m^2) with and without segregated cobalt in the optimal site using ABOP and DFT. The optimal grain boundaries in each of Σ4.1-Σ4.4 are highlighted in bold. Included are also the segregation energies.

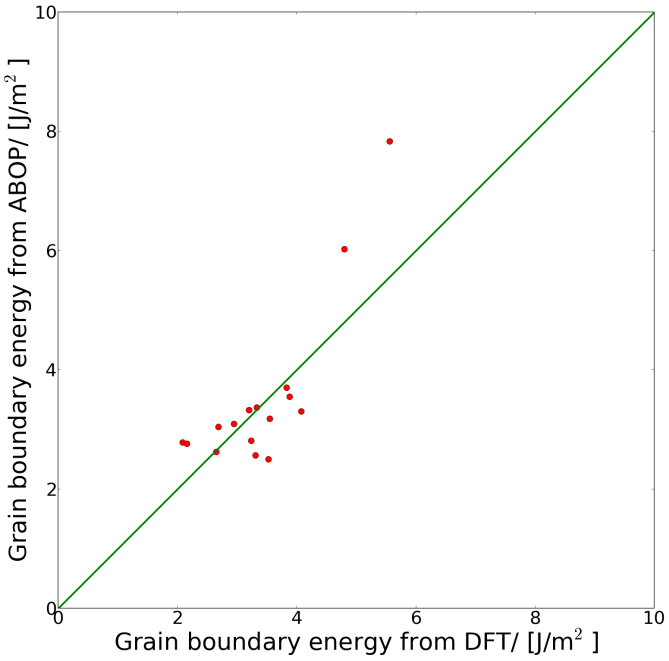

Figure 5.4: Comparison of grain boundary energies between ABOP and DFT.

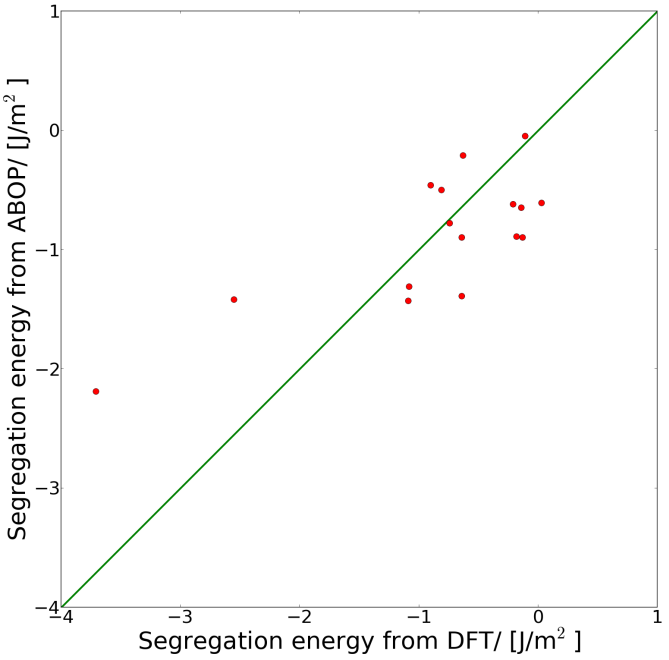

Figure 5.5: Comparison of segregation energies between ABOP and DFT.

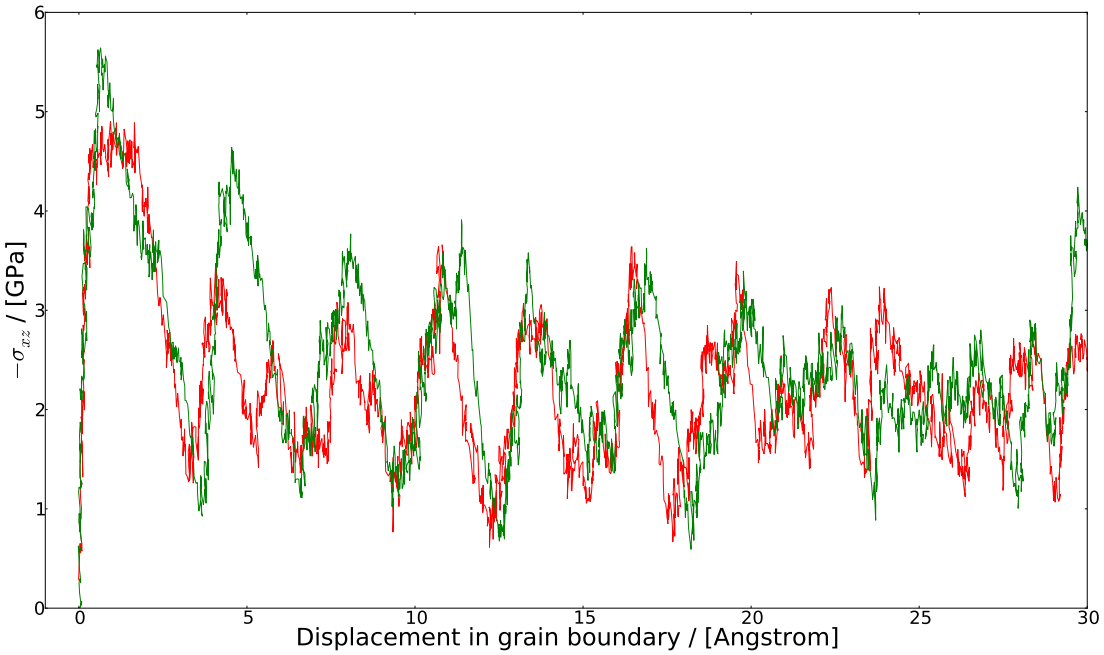

Figure 5.6: Comparison between two sliding simulation at the same temperatures but with different randomly distributed velocities.

5.3 Sliding and separation

This chapter starts with a part about the size of the system. Then there is a comparison between sliding and separation After that the dependency on temperature, velocity and stress will be studied. This will be done with clean grain boundaries. After that there will be a comparison between a clean grain boundary and a grain boundary with half a monolayer of cobalt.

5.3.1 System size

As a first step in the simulation process the size of the system to be used must be chosen. As described earlier the repeating unit in the direction of misfit is $37c$. It is natural to use only one such unit because of its large size. The resulting stress from simulations have been found to be sensitive to the initial conditions, which is illustrated in figure 5.6. The only difference between the two simulations is the randomly distributed velocities of the atoms for the given temperature. It is therefore necessary to make a large number of simulations to get good statistics. Therefore the sizes in the two other direction than the direction of misfit are chosen to be rather small. The size of the system perpendicular to the grain boundary was chosen to be half the size in the direction of misfit. In the direction of perfect match the size was chosen to be one fourth of the size in the direction of misfit. This resulted in a system of around 13 000 atoms. One of the grain boundary systems can be seen in figure 1.3.

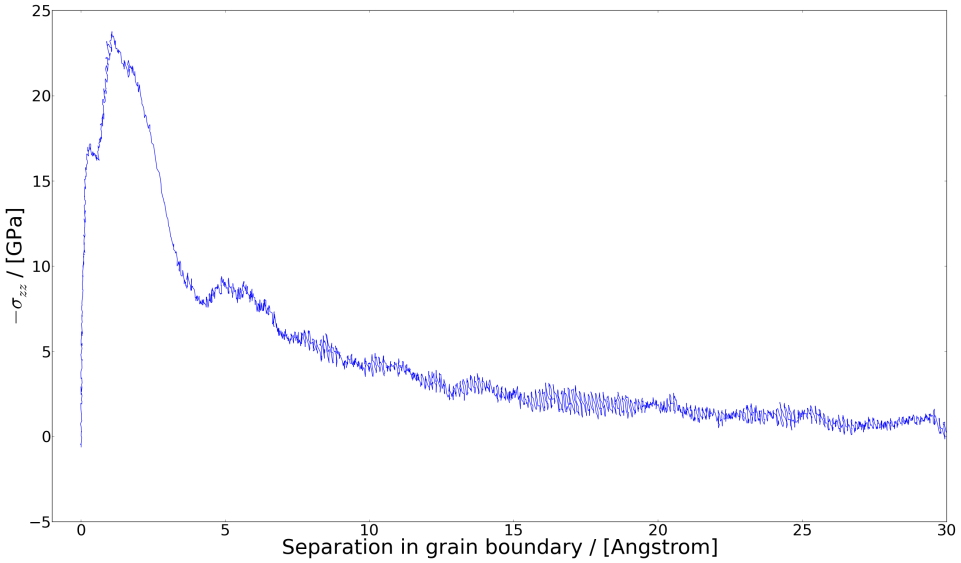

Figure 5.7: Stress versus separation curve of a separation simulation at 1500 K.

5.3.2 Comparison of sliding and separation

The are three possible directions in which the two slabs can be moved with respect to each other: first there is sliding in the direction of misfit, second there is sliding in the direction of perfect match and third there is separation perpendicular to the grain boundary. One simulation was performed in each of the three directions at 1500 K and at a velocity of $10\,\mathrm{m/s} = 0.1\,\mathrm{\AA/ps}$.
The resulting stress versus separation curve can be seen in figure 5.7. The peak stress is around 23 GPa. In figure 5.8 there are some figures showing the grain boundary separating. Atoms from the $(\bar{1}012)$ surface break off under separation while the prismatic surface remains intact with clusters of atoms from the other surface lying on top.
The resulting stress versus displacement curve for the sliding in the direction of perfect match can be seen in figure 5.9. The peak stress is approximately 13 GPa and the plateau stress is approximately 4 GPa.
The resulting stress versus displacement curve for the sliding in the direction of misfit can be seen in figure 5.10. The peak stress is around 5 GPa and the plateau stress is around 2 GPa. In figure 5.11 there are some figures showing the grain boundary slide in the direction of misfit. The outer layer of both surfaces become disordered during the sliding process. The outer layer of carbon in the $(\bar{1}012)$ surface tends to move along with the prismatic surface.
The peak stress for separation is significantly larger than for sliding. The peak and plateau stress are also about a factor two larger in the direction of perfect match than in the direction of misfit. This is significantly larger than the error from initial conditions. This is expected since the misfits should create possibilities for dislocation and defect movement which should lower the stress needed to slide. Based on these results the rest of the simulations will be sliding in the direction of misfit.

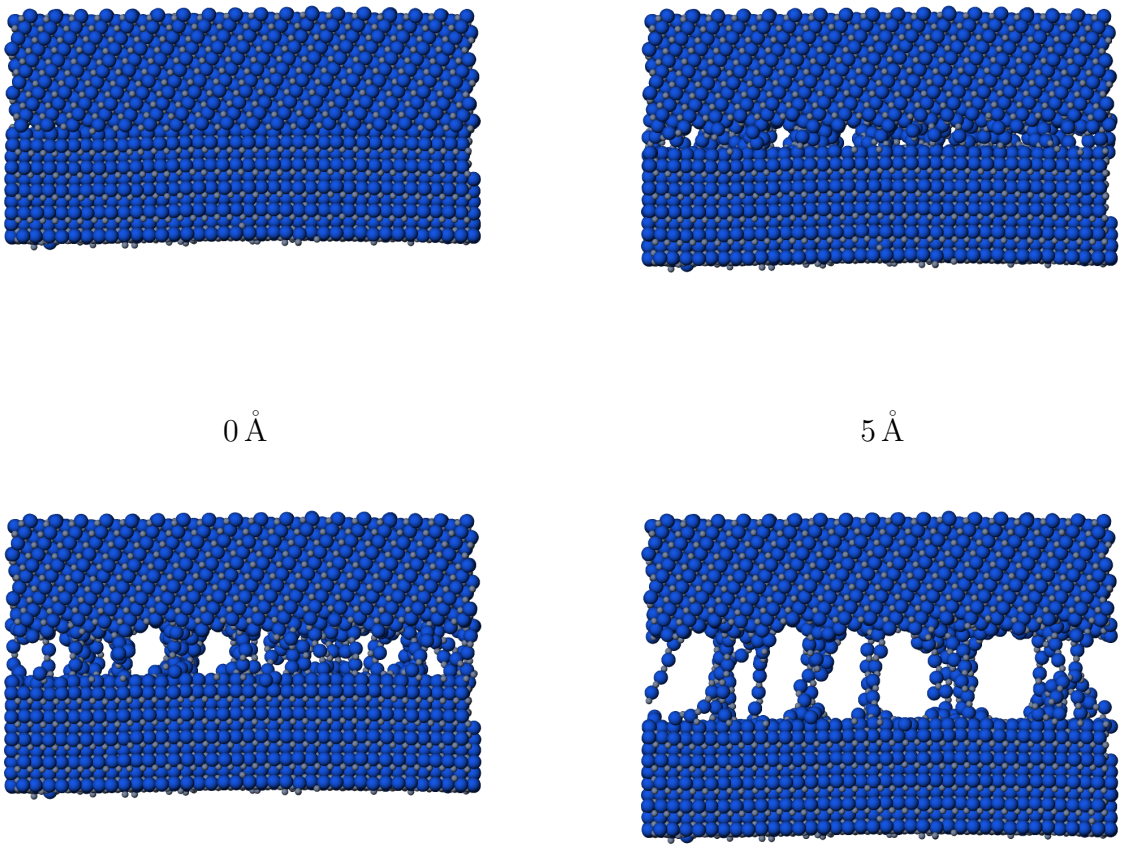

Figure 5.8: Figures of the system at different stages of the separation simulation. The pictures are at 0, 5, 10, and 20 Å separation.

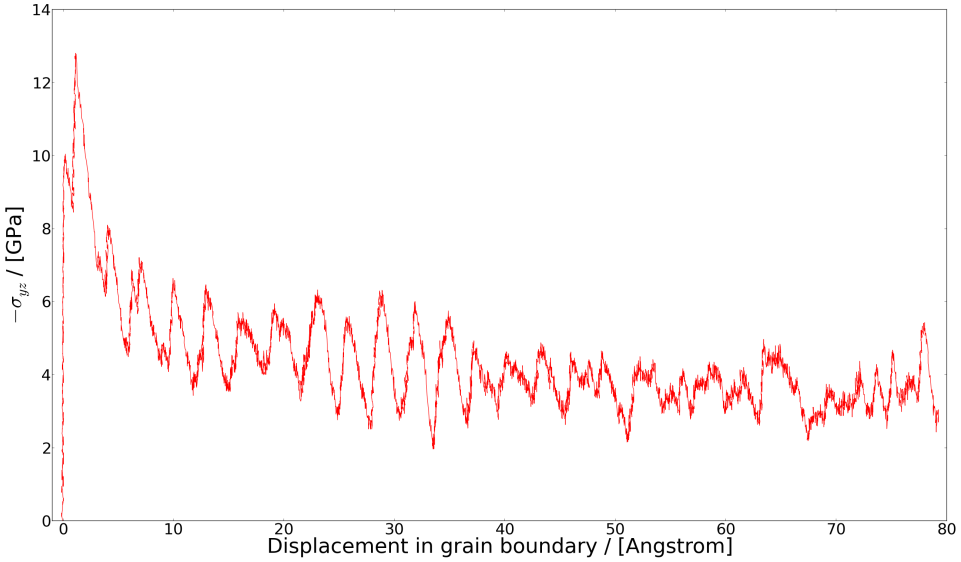

Figure 5.9: Stress versus displacement curve of sliding in the direction of perfect match at 1500 K.

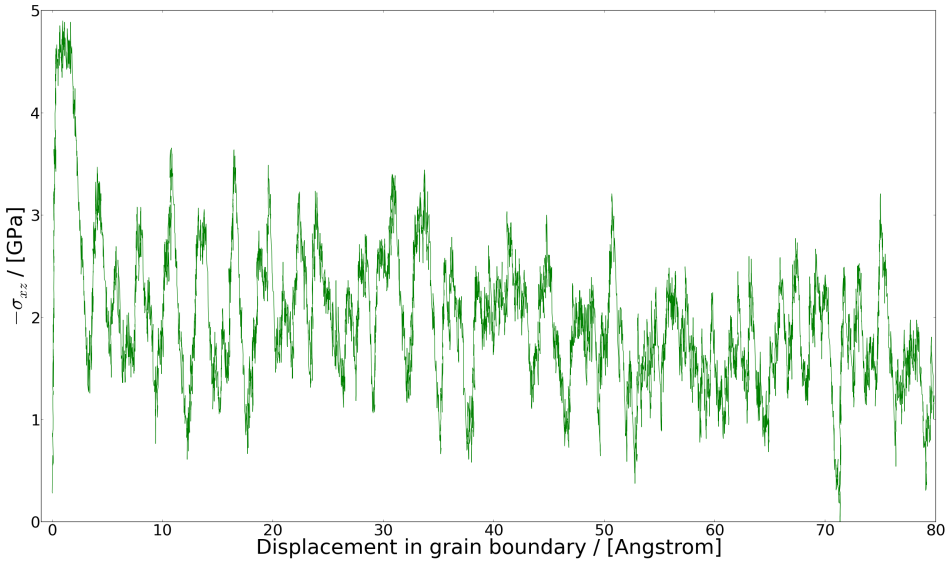

Figure 5.10: Stress versus displacement curve of sliding in the direction of misfit at 1500 K.

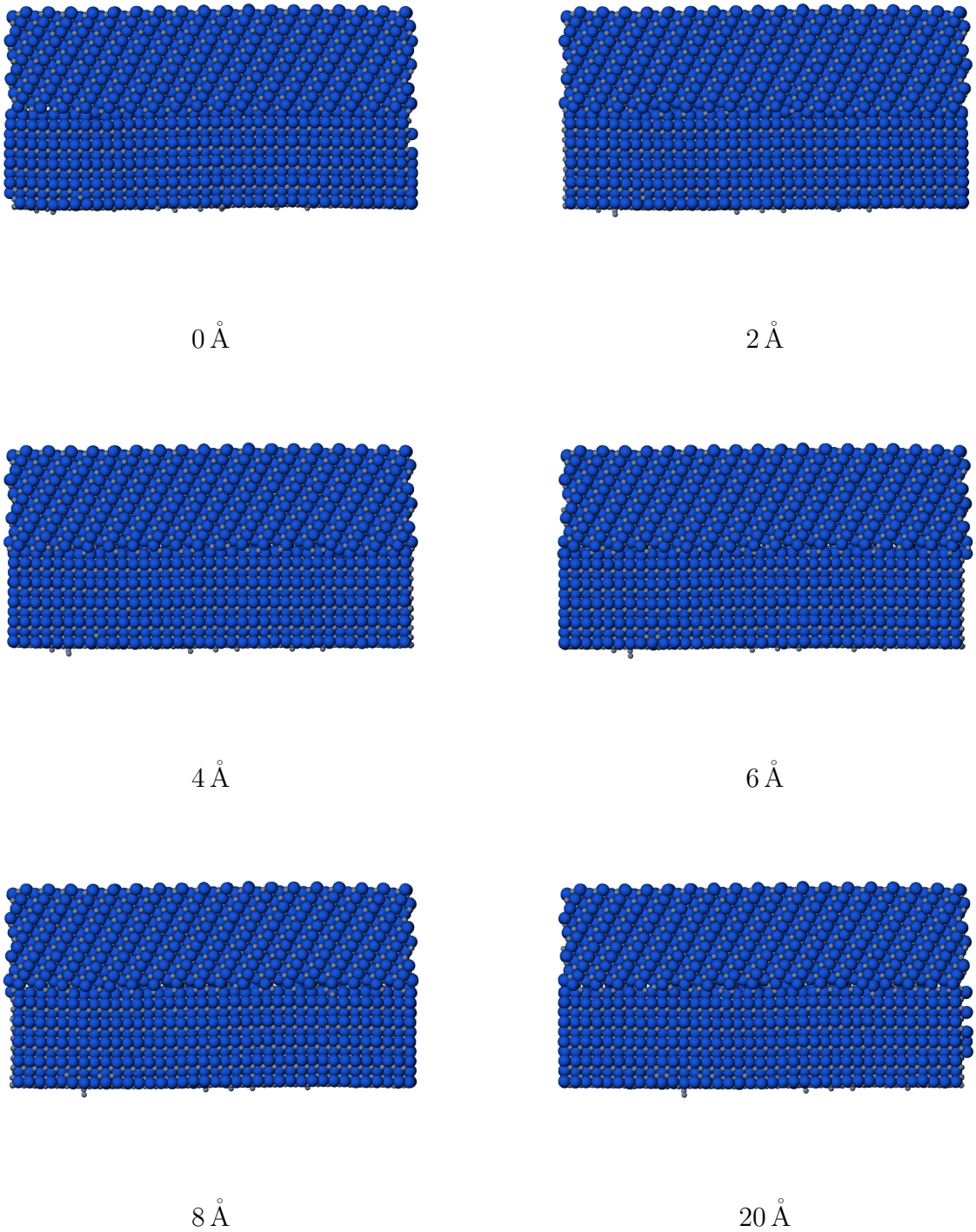

Figure 5.11: Figures of the system at different stages of the sliding simulation. The pictures are at 0, 2, 4, 6, 8, and 20 Å displacement.

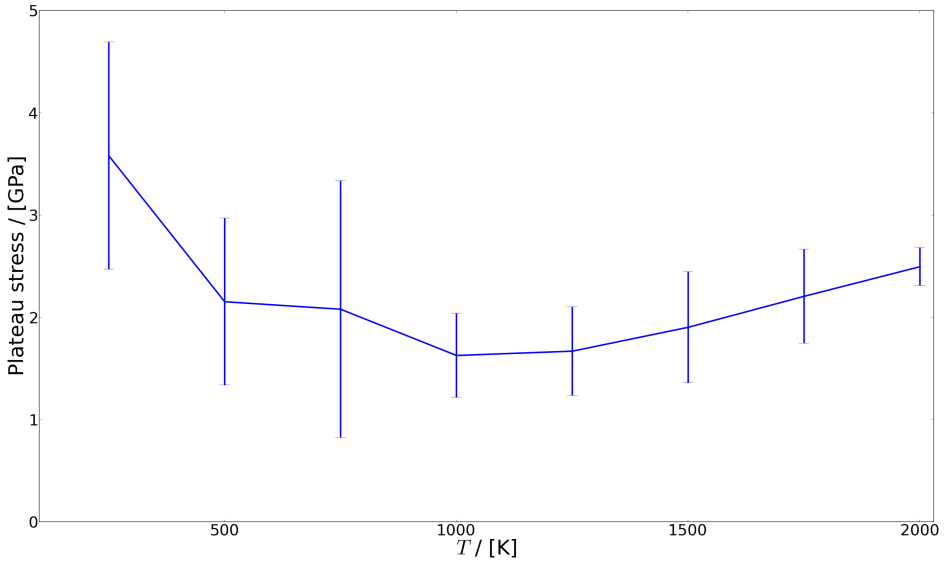

Figure 5.12: Plateau stresses at different temperatures with sliding velocity equal to 10 m/s. The errorbars represent a 95% confidence interval.

5.3.3 Temperature

The first dependency examined is how the sliding in the direction misfit is affected by temperature. Simulations were done for temperatures 250, 500, 750, 1000, 1250, 1500, 1750, and 2000 K. Statistics were made over 10 simulations at each temperature. The sliding was done at a velocity of 10 m/s. The resulting peaks and plateaus are plotted with error bars. A static simulation without MD to obtain the peak value at 0 K was also performed. Here, one of the outer regions was moved small steps and the system was minimized with respect to energy after each step. This type of simulation does not give a plateau value since there are no dynamics. Instead it simply flats out and oscillates at the peak value. This result was converged with respect to the step size. The results can be found in figures 5.12 and 5.13. The peak stress value decreases with increasing temperature. This demonstrates that the grain boundary is weakened with increasing temperature. The plateau stress value on the other hand decreases with increasing temperature for low temperatures but increases for higher temperatures. It is unclear what mechanism causes the the plateau stress to increase for high temperatures.

5.3.4 Velocity

One disadvantage with MD is that it operates on very small time scales. The simulation times are in the order of 1 ns. This means that the strain rate has to be large in order for the grains to move long enough during a simulation. In this thesis, velocities in the range $1 - 10$ m/s have been studied. The size of the system in the direction perpendicular to the grain boundary plain is approximately 50 Å. This gives a strain rate of approximately $0.2 \cdot 10^9 - 2 \cdot 10^9\,\mathrm{s}^{-1}$. The strain rates are only approximate since the size of the system

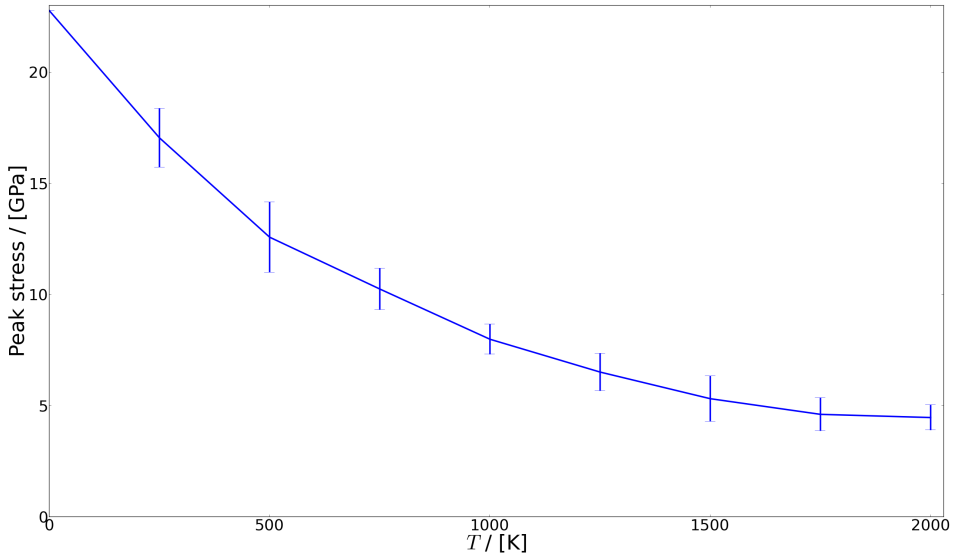

Figure 5.13: Peak stresses at different temperatures with sliding velocity equal to 10 m/s. The errorbars represent a 95% confidence interval.

changes with temperature and initial conditions. Statistics were made over 6 simulations at each velocity except for 10 m/s where 10 simulations where made. The aim is to see how the velocity affects the peak and plateau stress. This relation can then be extrapolated down to smaller velocities. The resulting plots can be seen in figures 5.14 and 5.15. The effect of the sliding velocity on the plateau stress is weak compared to the errors. It is therefore questionable to make an extrapolation of the plateau stress. The effect on the peak stress is however strong enough compared to the errors to show a clear trend.

5.3.5 Stress

The purpose of this part is to examine how the sliding is affected by a tensile or compressive stress perpendicular to the grain boundary. The aim is to be able to extrapolate peak and plateau stress values for different stresses. From previous simulations it has come clear that the stress perpendicular to the grain boundary is not zero but rather in the order of 0.5 GPa during sliding. This may be because the system does not have enough time to react to the stress when it is being strained . Because of this simulations will be done symmetrically around this unaltered system with respect to the stress. Statistics were made over 10 simulations at each applied stress. The results can be seen in figures 5.16 and 5.17
The effect of the applied stress on the shear stress is weak compared to the error. It is therefore not possible to draw any conclusions about the effect or making an extrapolation. To see larger effects on the shear stress larger applied stresses are needed.

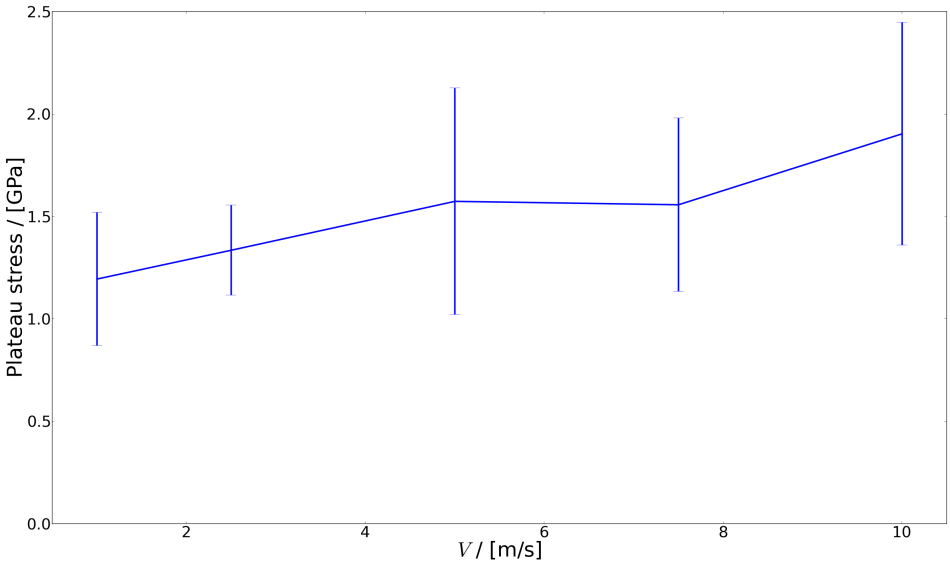

Figure 5.14: Plateau stresses at $T = 1500\,\mathrm{K}$ for different velocities (strain rates). The errorbars represent a 95% confidence interval.

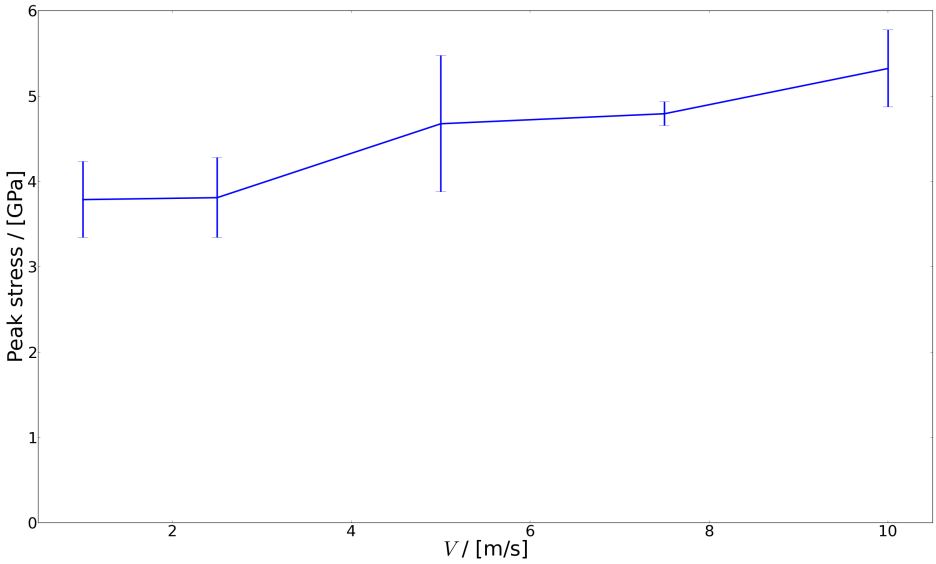

Figure 5.15: Peak stresses at $T = 1500\,\mathrm{K}$ for different velocities (strain rates). The errorbars represent a 95% confidence interval.

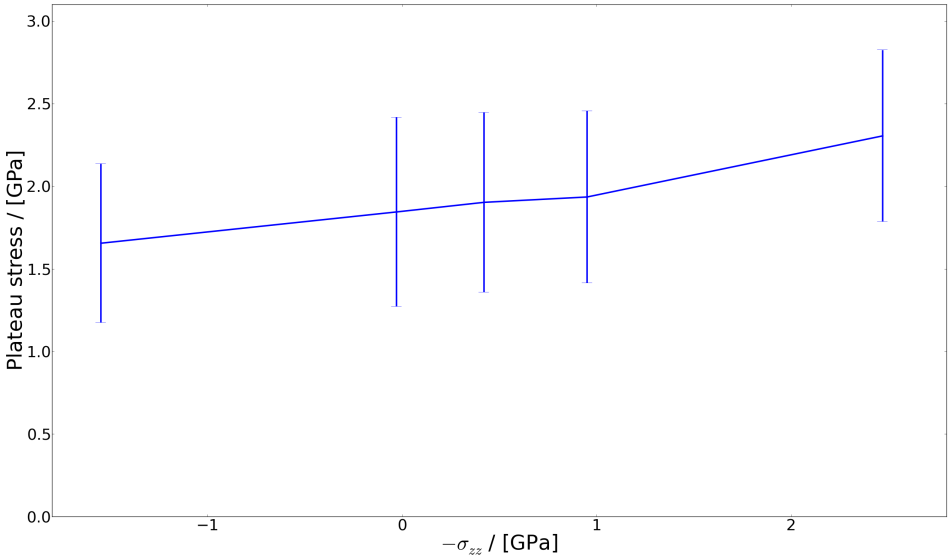

Figure 5.16: Plateau stresses at $T = 1500\,\mathrm{K}$ and with $V = 10\,\mathrm{m/s}$ for different applied tensile/compressive stresses. The errorbars represent a 95% confidence interval.

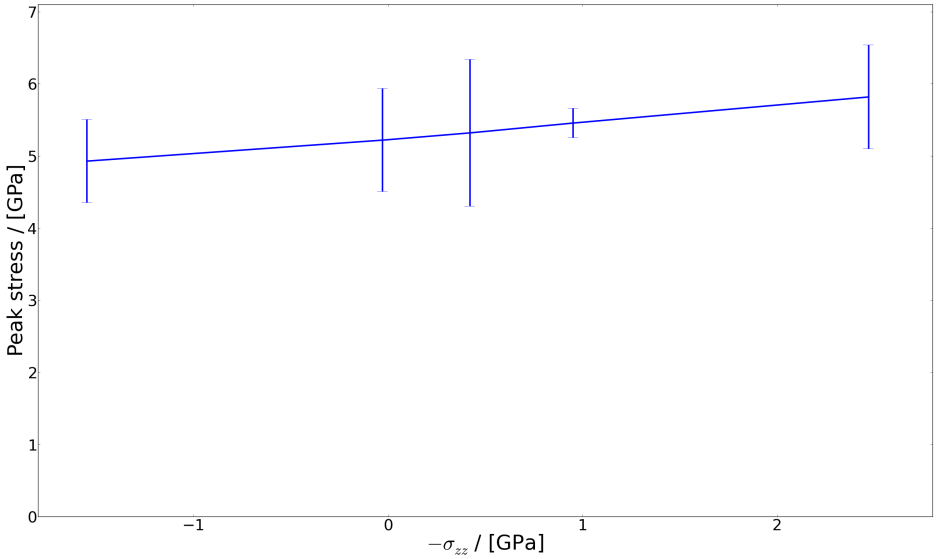

Figure 5.17: Peak stresses at $T = 1500\,\mathrm{K}$ and with $V = 10\,\mathrm{m/s}$ for different applied tensile/-compressive stresses. The errorbars represent a 95% confidence interval.

5.3.6 Sliding with half a monolayer of Co

Sliding in grain boundaries with half a monolayer of Co have been simulated. The simulations were done at $T = 1500\,\mathrm{K}$ and with a sliding velocity of $10\,\mathrm{m/s}$. The resulting mean plateau and peak stresses are $3.98 \pm 0.27\,\mathrm{GPa}$ and $8.09 \pm 0.27\,\mathrm{GPa}$ respectively. This should be compared with the same values for the clean grain boundary, $1.90 \pm 0.24\,\mathrm{GPa}$ and $5.32 \pm 0.45\,\mathrm{GPa}$. The stresses are about a factor 2 greater for the grain boundary containing segregated cobalt than for the clean grain boundary. The segregated cobalt thus strengthen the grain boundary with respect to sliding.

6. Conclusions

The segregation energies from the ABOP show that cobalt segregates into the grain boundaries to form half a monolayer. This is expected since the ABOP is fitted to electron structure calculations that have negative segregation energies for cobalt. The simulations also show that half a monolayer of cobalt strengthens the grain boundary: the stress under sliding is increased by a factor of two.
The misfit caused by $a \neq c$ lowers the the stress needed for sliding by a factor of two. It is thus significantly easier to slide along directions of misfit.
Simulations have shown that temperature and strain rate have a quite weak impact on grain boundary sliding. The applied external compressive/tensile stresses used in the simulations were too weak to show any clear trends on the stress during grain boundary sliding. The errors in the simulations were to large. To see larger changes in the stresses for sliding, simulations for larger compressive and tensile stresses need to be performed.
The stresses involved in grain boundary sliding and separation for clean grain boundaries and grain boundaries with half a monolayer of Co are on the order of 1–10 GPa. Furthermore, other simulations have shown that grain boundaries with a thin film of Co, i.e. several layers, substantially reduce the plateau stresses by a factor of 10–100 [13]. The occurrence of grain boundaries with thin films of Co is therefore likely to be crucial for the high temperature plastic deformation [22].
Mesoscopic simulations with implemented microscopic grain boundary laws will give more information about essential factors involved in plastic deformation. It is likely that more simulations need to be done on clean grain boundaries, grain boundaries with half a monolayer of Co and grain boundaries with thin films of Co.
Since the simulations in this thesis are done using a constant strain rate to give certain stresses when the system slides and separates it is important to make simulations with a constant stress to see if the resulting strain rate matches the ones in this thesis.
It is also important to the study the possibility of Co infiltration into clean grain boundaries to form thin films.

Bibliography

[1] S. Johansson. *A computational study of interface structures and energetics in cemented carbides and steels*. PhD thesis, Chalmers University of Technology, 2010.

[2] M. Christensen. *Strength and Stability of Interfaces in Cemented Carbides*. PhD thesis, Chalmers University of Technology and Göteborg University, 2004.

[3] `http://www.hero-m.mse.kth.se/page.php?pid=141` (2013/06/04).

[4] G. Östberg, K. Buss, M. Christensen, S. Norgren, H.-O. Andrén, D. Mari, G. Wahnström, and I. Reinbeck. Mechanisms of plastic deformation of WC-Co and Ti(C,N)-WC-Co. *International Journal of Refractory Metals & Hard Metals*, 26:135–144, 2006.

[5] F. Ercolessi. A molecular dynamics primer. `http://people.sc.fsu.edu/~jburkardt/pdf/ercolessi.pdf`(2013/05/21), 1997.

[6] D. Frenkel and B. Smit. *Understanding Molecular Simulations: From Algorithms to Applications*. Academic Press, 2002/1996.

[7] M. P. Allen and D. J. Tildesley. *Computer Simulation of Liquids*. Oxford University Press, 1987.

[8] J. Thijssen. Lecture notes advanced statistical mechanics ap3021g. `http://ocw.tudelft.nl/fileadmin/ocw/courses/AdvancedStatisticalMechanics/res00013/overview.pdf` (2013/05/21), 2008.

[9] E. B. Tadmor and R. E. Miller. *Modeling Materials: Continuum, Atomistic and Multiscale Techniques*. Cambridge University Press, 2011.

[10] `http://lammps.sandia.gov/` (2013/05/22).

[11] `http://lammps.sandia.gov/doc/pair_tersoff.html` (2013/05/21).

[12] J. Tersoff. New empirical approach for the structure and energy of covalent systems. *Phys. Rev. B*, 37:6991–7000, 1988.

[13] M. V. G. Petisme, S. A. E. Johansson, and G. Wahnström. Molecular dynamics simulation of wc/wc grain boundary sliding: the effect of thin cobalt films on sliding resistance. (2013). Proceedings of the 18st International Plansee Seminar.

[14] N. Juslin, P. Erhart, P. Träskelin, J. Nord, K. O. E. Henriksson, K. Nordlund, E. Salonen, and K Albe. Analytical interatomic potential for modeling nonequilibrium processes in the w-c-h system. *Journal of Applied Physics*, 98:123520, 2005.

[15] `http://www.benbest.com/cryonics/lessons.html`(2013/06/17).

[16] E. Lassner and W. D. Schubert. *Tungsten - Properties, Chemistry, Technology of the Element, Alloys and Chemical Compounds*. Kluwer Academic / Plenum Publisher, 1999.

[17] S. Hagége, G. Nouet, and Delavignette P. Grain boundary analysis in tem. iv. coincidence and the associated defect structure in tungsten carbide. *Phys. Status Solidi A*, 62:97–107, 1980.

[18] C.-S. Kim, T. R. Massa, and J. G. S. Rohrer. Interface character distributions in wc–co composites. *Am. Ceram. Soc.*, 91:996–1001, 2008.

[19] S. Johansson and M. Petisme, (2013). Chalmers University of Technology. Unpublished.

[20] D. S. Sholl and Steckel J. A. *Density Functional Theory: A practical introduction*. John Wiley & Sons Inc, 2009.

[21] F Guillermet. Thermodynamic properties of the Co-W-C system. *Metall. Trans. A*, 20:935, 1989.

[22] G. Östberg. *Changes in Microstructure During Plastic Deformation of Hardmetals*. PhD thesis, Chalmers University of Technology and Göteborg University, 2002.

CHALMERS UNIVERSITY OF TECHNOLOGY
SE 412 96 Göteborg, Sweden
Phone: + 46 - (0)31 772 10 00
Web: www.chalmers.se